Chemical Science

ROYAL SOCIETY OF CHEMISTRY

EDGE ARTICLE

View Article Online
View Journal | View Issue

Cite this: *Chem. Sci.*, 2025, **16**, 17276

All publication charges for this article have been paid for by the Royal Society of Chemistry

Enhancing photoredox catalysis by suppressing back electron transfer with the aid of a spin catalyst

Zhiqiang Dong,[ab] Chenli Chen,[c] Lingfang Chen,[d] Mingli Sun,[ab] Junzheng Zhan,[ab] Shen Zhou,[e] Lijia Cao,[ab] Jianyu Liu,[e] Shuming Bai,*[d] Jialong Jie,*[c] Hongmei Su,[c] Song Gao[fga] and Linan Zhou*[abh]

While organic dye-based photoredox catalysis provides a sustainable platform for inert bond activation, its efficiency remains limited by detrimental back electron transfer (BET) processes. Herein, we present a spin catalysis strategy that addresses this challenge by manipulating the spin kinetics of radical ion pairs (RIPs) using Gd-DOTA as a spin catalyst. In photocatalytic hydrodechlorination of methyl 4-chlorobenzoate, this approach achieved a remarkable spin catalysis effect (SCE) of 70%, accompanied by a 25-fold acceleration in reaction kinetics (65% conversion in 25 min *vs.* 640 min without spin catalyst). The generality of SCE was demonstrated across diverse substrates spanning varied functional groups and halides (Cl/Br/I). Through integrated time-resolved spectroscopic measurements and density functional theory calculations, we established a quantitative kinetic model revealing that the Gd(III) center promotes spin conversion of RIPs from singlet to triplet states, thereby effectively suppressing BET to enhance forward reaction flux. This work pioneers the integration of spin catalysis strategy into photoredox systems, offering both a mechanistic framework for spin-state manipulation in reaction engineering and a transformative kinetic approach to boost catalytic efficiency beyond current thermodynamic consideration solely based on redox properties.

Received 29th April 2025
Accepted 16th August 2025

DOI: 10.1039/d5sc03124a

rsc.li/chemical-science

Introduction

Over recent decades, photoredox catalysis has gained substantial attention in synthetic organic chemistry for its effectiveness in promoting radical-based organic transformations, enabling inert-bond activation and site-selective reactions under mild conditions.[1–4] While transition metal complexes, typically polypyridyl-coordinated Ir and Ru compounds, remain among the most widely used photoredox catalysts (PCs),[5–11] organic dyes offer an appealing alternative due to their low cost, ready availability, and reduced toxicity.[12–17] Notably, the weak spin–orbit coupling (SOC) of organic chromophores favors an effective excited state in singlet form, resulting in high redox potential without energy loss from intersystem crossing (ISC) processes. However, this characteristic also limits the photonic quantum efficiency, primarily due to significant back electron transfer (BET)[18,19] within the singlet germinated radical ion pairs (RIPs) generated from light-induced single-electron transfer (SET) between organic dye molecules and substrates (Fig. 1A). Therefore, suppressing the BET of singlet RIPs represents a promising strategy to enhance the photocatalytic efficiency of organic dyes.

Recently, electron spin control has gained extensive attention in enhancing photocatalytic performance,[20] with strategies including external magnetic field manipulation,[21] metal/nonmetal doping-induced spin polarization,[22] chiral-induced spin selectivity,[23] *etc.* Among them, spin regulation of radical pairs (RPs) – an important yet long-overlooked strategy – holds promise for improving reaction efficiency. The application of a third spin carrier, such as radicals or paramagnetic ions, for modulating the spin state of RPs, and thereby influencing the reaction path, has long been recognized as spin catalysis.[24–28] This effect is often observed in the photolysis of ketones,[29,30] where the approaching rate of initially pure triplet-state RPs

[a]*Spin-X Institute, South China University of Technology, Guangzhou 511442, China. E-mail: zhoulinan@scut.edu.cn*

[b]*School of Chemistry and Chemical Engineering, South China University of Technology, Guangzhou 510641, China*

[c]*College of Chemistry, Beijing Normal University, Beijing 100875, China. E-mail: jialong@bnu.edu.cn*

[d]*Beijing National Laboratory for Molecular Sciences, Key Laboratories of Organic Solids, Institute of Chemistry, Chinese Academy of Sciences, Beijing 100190, China. E-mail: baishuming@iccas.ac.cn*

[e]*Institute for Quantum Science and Technology, College of Science, National University of Defense Technology, Changsha 410003, China*

[f]*Key Laboratory of Bioinorganic and Synthetic Chemistry of Ministry of Education, LIFM, School of Chemistry, IGCME, Sun Yat-Sen University, Guangzhou 510275, China*

[g]*Key Laboratory of Bioinorganic and Synthetic Chemistry of Ministry of Education, Guangdong Basic Research Center of Excellence for Functional Molecular Engineering, School of Chemistry, Sun Yat-Sen University, Guangzhou 510275, China*

[h]*State Key Laboratory of Luminescent Materials and Devices, South China University of Technology, Guangzhou 510641, China*

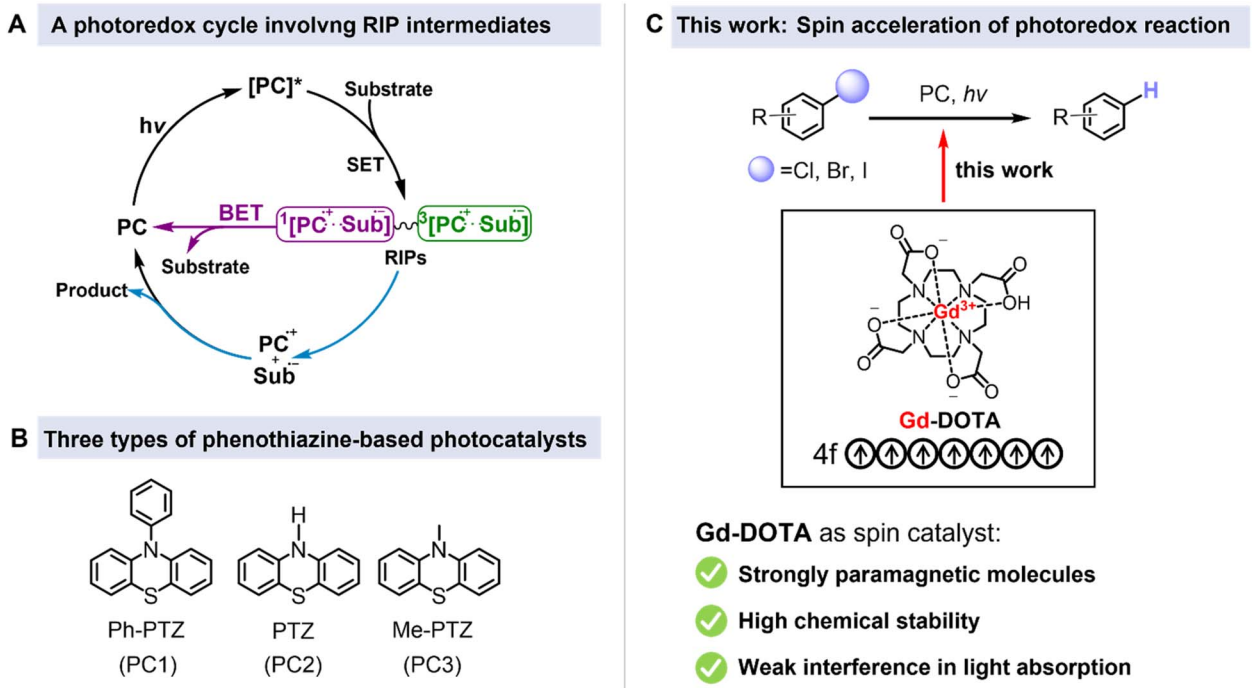

Fig. 1 Proposal of spin catalyzing photoredox reaction. (A) Scheme of a photoredox cycle emphasizing the underrepresented radical ion pairs (RIPs) intermediates and back electron transfer process. (B) Structures of the photocatalysts intestigated in this work. (C) Application of Gd-DOTA as a spin catalyst for promoting the photoredox transformations *via* spin modulation in this work.

towards spin equilibrium with more singlet population is accelerated. This shift enhances the likelihood of RPs recombination and cage products formation, governed by the Pauli exclusion principle. Conversely, for processes involving RPs or RIPs initially born in the singlet state, spin catalysts should boost the transition rate to the triplet state, thus inhibiting the back process.

Herein, we prove this idea by showing that the efficiency of a photoredox reaction mediated by an organic dye can be significantly enhanced with the simple addition of a gadolinium- based spin catalyst. Photoredox hydrodehalogenation of aromatic halide was chosen as a model reaction (Fig. 1C). Light-driven activation of carbon–halogen (C–X) bonds has emerged as a powerful strategy for constructing new chemical bonds in valuable pharmaceutical and industrial intermediates, as well as for degrading polyhalogenated aromatic pollutants.[31–38] Although the great abundance of chlorinated compounds makes them highly desirable substrates, their inertness with high reduction potentials (−1.7–2.5 V *vs.* the saturated calomel electrode) hinders their widespread application.[39] Organic dyes with a strongly reducing singlet excited state, such as phenothiazine (Fig. 1B), have shown promise in facilitating the dissociation of these otherwise inert C–Cl bonds, though typically with limited efficacy.[40] We aimed to accelerate the transformation of this photoredox organic reaction using paramagnetic spin catalyst-Gd-DOTA (DOTA = 1,4,7,10-tetraazacyclododecane-1,4,7,10-tetraacetic acid, Fig. 1C; mass spectrum in Fig. S1). Gadolinium center with a high-spin ground state (S = 7/2) is expected to exhibit superior spin catalytic effect.[30,41,42] The chelating structure of Gd-DOTA exhibits enhanced chemical stability and reduced interference with the reaction compared to free ions. This marks the first attempt to utilize a Gd(III) macrocyclic complex as a spin catalyst to promote reaction efficiency of photoredox organic transformations.

Experimental section

Materials

All reagents and solvents were commercially available (Adamas-beta®, Adamas-life® and Energy Chemical, *etc.*) and used without further purification unless otherwise noted.

Synthesis of spin catalysts

1.4,7,10-Tetraazacyclododecane-1,4,7,10-tetraacetic acid (DOTA).[43] Cyclen (500 mg, 2.90 mmol, 1.0 eq.) was dissolved in 5 mL of H_2O and stirred, after which a 1 M HCl solution was added to adjust the pH to 8.5. Chloroacetic acid (1.21 g, 12.8 mmol, 4.4 eq.) was then added, and the mixture was heated to 80 °C with continuous stirring. The pH was maintained between 8.5 and 10 by periodically adding a few drops of 5 M KOH solution. The reaction mixture was refluxed overnight. The pH was subsequently reduced to 2 using 5 M HCl, resulting in the formation of a solid precipitate. The precipitate was filtered and purified by recrystallization from HCl (yield: 80%). ^{1}H-NMR: (400 MHz, D_2O) δ = 3.16 (bm, 16H) ppm, 3.95 (bm, 8H) ppm. LCMS (*m*/*z*): (ES-API, ACN/H_2O): calculated for $[C_{16}H_{28}N_4O_8]^+$: 405.2; found 405.2.

Gd-DOTA.[44] $GdCl_3 \cdot 6H_2O$ (50.5 mg, 136 μmol, 1.1 eq.) was added to a stirred solution of DOTA (50.0 mg, 124 μmol, 1.0 eq.) in 5 mL of H_2O, and the pH was adjusted to 6.5–7.0 using 1 M KOH. The mixture was stirred at 60 °C for 24 hours, followed by filtration through a 0.22 μm syringe filter. The resulting compound was obtained as a white flake solid after lyophilization. This solid was dissolved completely in methanol, then precipitated by adding ten times the volume of ether. The precipitate was collected by centrifugation, and the supernatant was discarded. This process was repeated three times. The final product, a white fluffy powder, was obtained by drying the precipitate (yield: 70%). MS (*m*/*z*): (ESI, ACN/H_2O) calculated for $[C_{16}H_{24}N_4O_8Gd]^-$: 558.1; found 558.1.

Y-DOTA. The synthesis method is similar to Gd-DOTA. MS (*m*/*z*): (ESI, ACN/H_2O) calculated for $[C_{16}H_{25}N_4O_8Y]^+$: 491.1; found 491.1.

Photocatalytic measurements

Photocatalytic experiments were performed using a parallel light reactor (Roger RLH-18CU) with an internal 365 nm LED light. The photocatalytic reactions were conducted in mixed solvent DMSO : H_2O (9 : 1, v/v) without heating in air. Ultrasonic-assisted dissolution was necessary at a Gd-DOTA concentration of 12 mol%, due to the solubility issue of the Gd-DOTA. During the experiment, the light intensity and temperature conditions were consistent for all samples. The products were analyzed using gas chromatography (GC) (SHIMADZU 2014C) equipped with a flame ionization detector (FID). A PC-5 capillary column (15 m × 0.25 mm, 0.25 μm film thickness) was used with Ar as the carrier gas. The FID was maintained at 290 °C, with hydrogen and air flow rates of 40 and 400 mL min^{-1}, respectively. Data were acquired and analyzed using SHIMADZU LabSolutions software. The yield and conversion of the substances in this work were all obtained from quantitative analysis of GC data.

EPR measurements

The cw-EPR spectra were measured on a Bruker Magnettech ESR5000 spectrometer and the spectrometer works at X-band (9.48 GHz). The cw-EPR spectra were simulated using an EasySpin[45] toolbox based on MATLAB R2024a. The term lwpp stands for line with for peak-to-peak isotropic broadening, in our case, Gaussian broadening is considered.

Viscosity measurements*Viscosity measurements*

Viscosity was measured using an NDJ-5Spro micro viscometer (XIUILAB, China) with a sample volume of 20 mL, a speed of 60 rpm, and a range of 10 m Pas (0.1 P). The measurements were conducted in a thermostatic water bath to determine viscosity at different temperatures.

Cyclic voltammetry (CV) measurements

CV measurements were performed on a CHI760E electrochemical workstation using a three-electrode system, consisting of a 3 mm diameter glassy carbon electrode, a saturated calomel electrode (SCE) and a platinum wire. The electrolyte was an anhydrous acetonitrile solution containing 0.1 M tetrabutylammonium hexafluorophosphate, which was degassed with high-purity nitrogen for 15 min prior to testing. CV scans were conducted at a scan rate of 100 mV s^{-1} over a potential range from −2.5 V to 0 V. The peak potentials were calibrated using the redox potential of ferrocene (Fc/Fc* = 0.32 V *vs.* SCE), after which the reduction peak potentials and peak currents of other samples were recorded.

Time-resolved spectroscopy measurements

Streak camera. The high-resolution streak camera system measures time-resolved luminescence spectra through the combined operation of a streak camera (C10910-05, Hamamatsu) with a CMOS camera (C13440-20CU) and a spectrometer (HRS-300-S). The streak camera offers two scanning modes: a fast-scanning mode with a minimum time window of 70 ps and a slow-scanning mode with a minimum time resolution window of 1 ps. The maximum time resolution of the streak camera in single-pulse mode is 1.37 ps. The 355 nm excitation light is generated by an OPA (TOPAS-C, Coherent Inc.), and the fundamental pulse (800 nm, 40 fs, 1 kHz) is produced by a Ti:sapphire laser system (Coherent Astrella).

Laser flash photolysis. Time-resolved laser flash photolysis (LFP) was used to measure the transient UV-vis absorption spectra. Briefly, an Edinburgh LP980 spectrometer (Edinburgh Instruments Ltd) is synchronized with a commercial Nd:YAG laser (Lab 170, Spectral Physics Inc.). The excitation wavelength is 355 nm (1 Hz, fwhm ≈ 7 ns). Each measurement was performed in a quartz cuvette with 1 cm path length at room temperature. The analyzing light was from a 150 W pulsed xenon lamp. A monochromator equipped with a photomultiplier for collecting the spectral range from 300 to 700 nm was used to analyze transient absorption spectra. The signals from the photomultiplier were displayed and recorded as a function of time on a 100 MHz (1.25 Gs per s sampling rate) oscilloscope (Tektronix, TDS 3012C), and the data were transferred to a personal computer. Data were analyzed by the online software of the LP980 spectrophotometer. The fitting quality was judged by weighted residuals and reduced χ^2 value.

Femtosecond transient absorption. The femtosecond transient absorption spectra were measured using a femtosecond transient absorption spectrometer (Harpia-TA, Light Conversion). The fundamental pulses (800 nm, 40 fs, 1 kHz) were generated with a Ti:Sapphire laser system (Coherent Astrella) and split by a beam splitter to generate the pump and probe beams. A small fraction of the fundamental pulses was sent to a computer controlled optical delay line and then focused onto a CaF_2 plate to generate the white light continuum probe beam. The rest of the fundamental pulses were sent to the optical parametric amplifier (TOPAS-C, Coherent Inc.) to generate the 355 nm pump beam, which was chopped at 500 Hz. To avoid anisotropic signals, the polarizations of pump and probe beams were set to the magic angle (54.7°) in all measurements. The focused signal and pump beams were overlapped into a fused silica cuvette with a 1 mm beam path length. The differential

absorbance ΔA (t, λ) obtained from the femtosecond transient absorption spectra as a function of wavelength and time delay was analyzed using the Glotaran program. All experiments were carried out at room temperature.

Quantum mechanics calculation

Density functional theory (DFT) calculations were performed with the Gaussian16 program suite (Revision A.03).[46] All calculations were carried out with UB3LYP functional.[47] The geometry optimizations of Sub 1–4 and PC1–PC3 in DMSO were performed at UB3LYP/def2-TZVP level, and vibrational frequency calculations were carried out to verify the obtained stationary points as local minima (with no imaginary frequency). The hyperfine coupling constants (HFCCs) in DMSO were calculated at UB3LYP/pcH-2 level. The isotropic HFCCs are related to the spin density at the corresponding nucleus N, and the conversion factors for the different nuclei are given by the expression:[48]

$$A_{ik}(N) = 142.770\ \langle S_z \rangle^{-1} g_N \rho(N)$$

where $\rho(N)$ is expressed in a.u. and A_{ik} is obtained from the quantum chemical calculation, with the unit of Gauss.

Results and discussion

Proof and evaluation of spin catalysis effect in photoredox reaction

Based on UV-vis absorption spectra (Fig. S2), all photocatalysts exhibit effective absorption up to 400 nm, indicating feasible excitation by 365 nm light. Taking Ph-PTZ as an example, when a 365 nm LED lamp is used as the light source, the hydrodechlorination of methyl 4-chlorobenzoate (Sub 1) proceeds efficiently in the presence of DIPEA (the sacrificial reducing agent; Table 1, entry 1). The absence of light, Ph-PTZ, or the reducing agent leads to no observable formation of the desired product (Table 1, entries 2–4), suggesting the indispensable role of the three components. Notably, the addition of Gd-DOTA to the photocatalytic system enhances the forward conversion of the reaction (Table 1, entry 5). Given that Gd-DOTA barely absorbs light with wavelengths above 300 nm (Fig. S3), minimal competition for 365 nm photons between Gd-DOTA and Ph-PTZ is expected. Moreover, no reaction was observed in the presence of Gd-DOTA without Ph-PTZ (Table 1, entry 6), which excludes the possibility of Gd-DOTA acting as a photocatalyst. Replacing the paramagnetic Gd-DOTA with diamagnetic Y-DOTA results in only a trivial enhancement of the photocatalytic activity (Table 1, entry 7 and Fig. S4), highlighting the essential role of spin in promoting the photoredox reaction. By contrast, while $GdCl_3$ also exhibit some photocatalytic enhancement, its effect is markedly weaker than that of Gd-DOTA (Fig. S5). This stark difference is likely due to unfavorable chemical interactions between free Gd^{3+} ions and reaction intermediates—highlighting the distinct advantages of chemically inert Gd-DOTA in achieving efficient spin catalysis and serving as an ideal object for studying pure spin effects. We further compared the spin catalysis effect of Gd-DOTA for the three different photocatalysts, with same absorbance at the excitation wavelength *via* adjusting PC concentrations (Fig. S2). As shown in Fig. 2, Gd-DOTA significantly enhances the performance of the PC1 compared to the other two.

We further investigated the effect of varying Gd-DOTA concentrations on the photocatalytic performance of Ph-PTZ. It was observed that the conversion of Sub 1 asymptotically approaches 65% over a 640-minute reaction time (Fig. 3A, hollow squares). In the presence of 5 mol% Gd-DOTA, the reaction time required to achieve the same conversion was reduced to just 100 minutes (Fig. 3A, pale blue), less than 1/6 of the time needed without Gd-DOTA. When the concentration of

Table 1 Validation of spin catalysis effect through controlled variable experiments

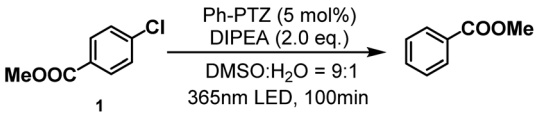

Entry	Variation from standard conditions	Yield[b]/%
1	None	33
2	Without light	0
3	Without Ph-PTZ	0
4	Without DIPEA[a]	0
5	With Gd-DOTA (10 mol%)	51
6	Gd-DOTA without Ph-PTZ	0
7	With Y-DOTA (10 mol%)	34

[a] DIPEA: *N*,*N*-diisopropylethylamine. [b] Quantitative analysis of all substances was performed by GC. Reaction conditions: a 10 mL reaction volume [(DMSO : H_2O) = 9 : 1 (v : v)] of substrate (Sub 1, 0.1 M), Ph-PTZ (5 mol%), DIPEA (2 equiv.) in air with irradiation by 365 nm LED (4 W cm^{-2}).

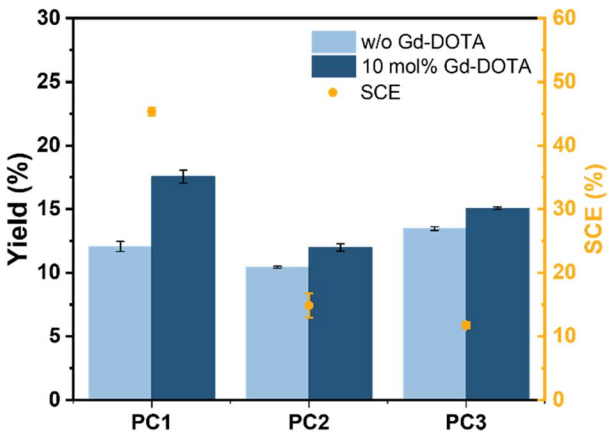

Fig. 2 Spin catalysis effect for different photosensitizers in photocatalytic hydrodechlorination of methyl 4-chlorobenzoate. Reaction conditions: 10 mL reaction solution [DMSO : H_2O = 9 : 1 (v/v)] with 0.1 M substrate, appropriate amount of photocatalyst and 2 equiv. DIPEA, under irradiation by 365 nm LED (4 W cm^{-2}) in air for 5 minutes. The concentrations of photocatalyst were set to 5 mol%, 3 mol% and 10 mol% for PC1, PC2 and PC3, respectively, to achieve same absorbance at 365 nm excitation.

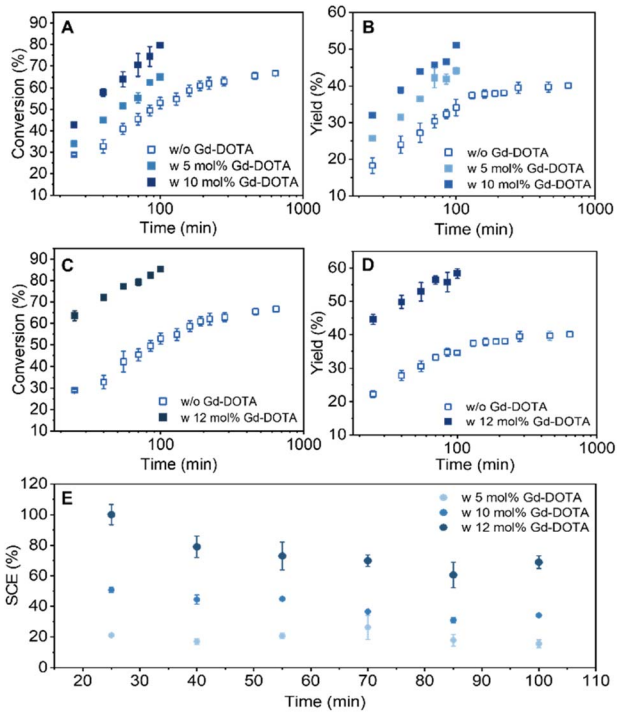

Fig. 3 Dependence of SCE on concentration of spin catalyst Gd-DOTA. The progression of (A) reaction conversion and (B) yield over time, without and with Gd-DOTA at concentrations of 5 mM and 10 mM, respectively, and room temperature. The progression of (C) reaction conversion and (D) yield over time, without and with Gd-DOTA at concentrations of 12 mM and reaction temperature of 60 °C. (E) SCE of Gd-DOTA at varied concentration of 5, 10 and 12 mM over reaction time. Reaction conditions: 10 mL reaction solution [DMSO : H_2O = 9 : 1 (v : v)] with 0.1 M methyl 4-chlorobenzoate, 5 mol% PC1 and 2 equiv DIPEA under irradiation by 365 nm LED (4 W cm^{-2}) in air. The quantitative results were determined by GC.

Gd-DOTA was increased to 10 mol%, the required time was reduced more than tenfold to just 55 minutes, and the conversion reached 80% within 100 minutes (Fig. 3A, dark blue). At 12 mol% Gd-DOTA, the time to achieve a 65% conversion was further reduced to only 25 minutes, which otherwise requires 640 minutes without Gd complex, shortened by 25 times. The conversion and yield increased from 53% and 34% to 85% and 58%, respectively, over a 100-minute period (Fig. 3B–D). A reaction order analysis indicates first-order reaction kinetics both in the absence and presence of Gd-DOTA, with the rate constants exhibiting a linear dependence on Gd-DOTA concentration within the experimentally accessible range in this study (Fig. S6). This finding supports that Gd-DOTA does not alter the reaction mechanism but instead acts exclusively as a spin catalyst, and a diffusion-controlled mechanism for spin catalysis is implied.

Spin catalysis effect (SCE) is defined based on the yield of the target product, with the formula:

$$\mathrm{SCE} = [\mathrm{Yield}^{\mathrm{w}} - \mathrm{Yield}^{\mathrm{w/o}}]/\mathrm{Yield}^{\mathrm{w/o}} \times 100\%$$

where $\mathrm{Yield}^{\mathrm{w}}$ and $\mathrm{Yield}^{\mathrm{w/o}}$ represent the yield in the present and absence of Gd-DOTA, respectively. The SCEs for 5 mol%, 10 mol%, and 12 mol% Gd-DOTA were determined to be approximately 23%, 48%, and 70%, respectively (Fig. 3E). The positive correlation between SCE and the concentration of Gd-DOTA suggests that the promotion effect of Gd-DOTA in photoredox reaction is likely governed by a diffusion-controlled mechanism (*vide infra*). This diffusion-controlled behavior is also supported by James D's theory of spin-center exchange.[49,50]

Mechanistic studies with time-resolved spectroscopic measurements

To better understand how the spin of Gd-DOTA modulates the reaction and enhances photocatalytic performance, we conducted ultrafast time-resolve absorption and emission spectroscopic studies to elucidate the underlying mechanism and dynamics of the photoredox hydrodechlorination of Sub 1 using Ph-PTZ as the photocatalyst.

Fig. 4A shows the femtosecond transient absorption (fs-TA) of Ph-PTZ following photoexcitation. Initially, two broad absorption bands, attributed as the singlet excited state of Ph-PTZ (^{1}Ph-PTZ*), emerge at 390 and 650 nm, which exhibit a decay on the nanosecond timescale, concurrent with the appearance of a new absorption band at 460 nm (Fig. 4B). This eventual spectrum at 7 ns with 460 band being indicative of a longer-lived transient (Fig. 4C), closely matches the reported spectrum for triplet of Ph-PTZ (^{3}Ph-PTZ*),[51] confirming the assignment of this species to ^{3}Ph-PTZ*. The fitted lifetime of ^{1}Ph-PTZ* (Fig. 4D) is consistent with our time-resolved emission data (Fig. S7). In contrast, the fs-TA spectra of Ph-PTZ$^+$ Sub 1 differ significantly from those of Ph-PTZ (Fig. 4E). The interaction with Sub 1 notably accelerates the decay of ^{1}Ph-PTZ*, accompanied by the emergence of a new spectral feature within 30 ps, characterized by bands around 390, 510, and 650 nm (Fig. 4F). These features are assigned as exciplex between ^{1}Ph-PTZ* and Sub 1 (^{1}Ph-PTZ*···Sub 1). Thereafter, from 30 to 200 ps, ^{1}Ph-PTZ*···Sub 1 decays gradually, leading to a second spectrum. This new spectrum, with a band at 510 nm and a shoulder around 460 nm, is attributed to the RIP species, Ph-PTZ$^{\bullet+}$···Sub 1$^{\bullet-}$. After 200 ps, Ph-PTZ$^{\bullet+}$···Sub 1$^{\bullet-}$ undergoes decay, resulting in the formation of the eventual long-lived species with bands around 460 and 510 nm, corresponding to ^{3}Ph-PTZ* and free Ph-PTZ$^{\bullet+}$ (Fig. 4G), respectively.[51–53] The coexistence of both ^{3}Ph-PTZ* and free Ph-PTZ$^{\bullet+}$ suggests that for the decay of Ph-PTZ$^{\bullet+}$···Sub 1$^{\bullet-}$, in addition to the BET pathway to the ground state, two additional decay pathways are present: charge recombination to ^{3}Ph-PTZ*, and escape from the solvent cage to form free Ph-PTZ$^{\bullet+}$ and Sub 1$^{\bullet-}$. The transient spectra for Ph-PTZ were globally fit with three time constants: 7 ps, 46 ps, and 275 ps corresponding to the decay of ^{1}Ph-PTZ*, the decay of ^{1}Ph-PTZ*···Sub 1, and the decay of Ph-PTZ$^{\bullet+}$···Sub 1$^{\bullet-}$, respectively (Fig. 4H).

Furthermore, using the extinction coefficients of Ph-PTZ$^{\bullet+}$, reported by the literature[54] and the extinction coefficient of ^{1}Ph-PTZ* and ^{3}Ph-PTZ* estimated by us (refer to ST 1, Fig. S8), we further quantified the relative contributions and rates for the

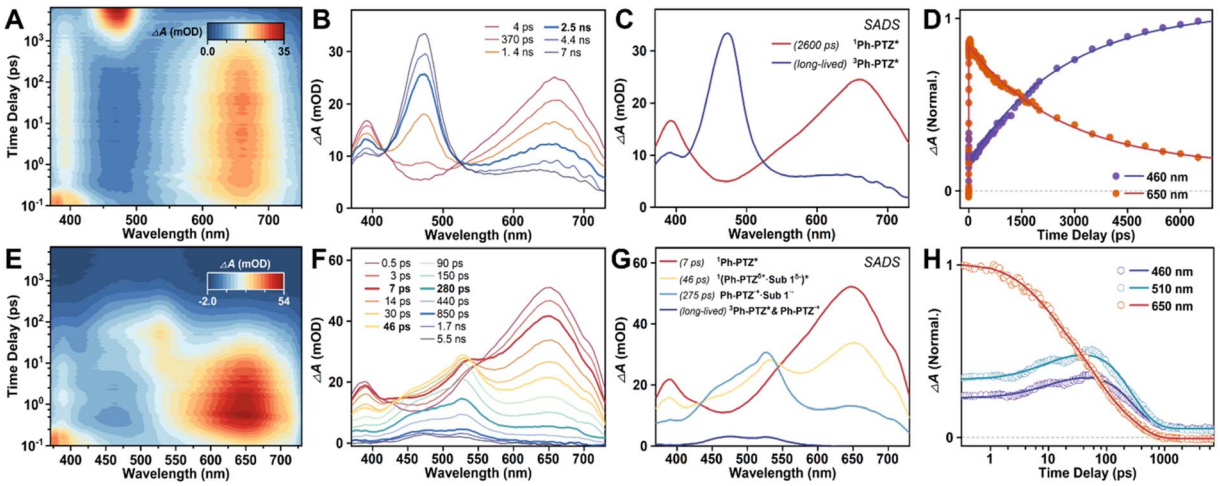

Fig. 4 Time-resolved spectroscopic experiments. (A) Transient absorption two-dimension (2D) contour map; (B) transient absorption spectra (TAS) at typical delay times; (C) Species-Associated Differential Spectra (SADS) obtained from the global analysis of the transient spectra; (D) time traces at typical wavelengths (dots), together with the fits (lines) from the global analysis. Experimental conditions: 350 nm laser excitation, Ph-PTZ (7.5 mM) in a mixture solvent of DMSO : H_2O = 9 : 1 (v : v); (E) transient absorption 2D contour map; (F) TAS at typical delay times; (G) SADS obtained from the global analysis of the transient spectra; (H) time traces at typical wavelengths (dots), together with the fits (lines) from the global analysis. Experimental conditions: 350 nm laser excitation, Ph-PTZ (5 mM) + Sub 1 (1 M) in a mixture solvent of DMSO : H_2O = 9 : 1 (v : v).

three decay pathways of Ph-PTZ$^{\bullet+}$···Sub 1$^{\bullet-}$ (Fig. 5A): (1) BET within the RIPs, with $k_{BET} = 3.2 \times 10^9$ s^{-1}, leading to an ineffective photoredox cycle; (2) diffusion-controlled separation of RIPs to form free Ph-PTZ$^{\bullet+}$ and Sub 1$^{\bullet-}$, with $k_{dif} = 3.2 \times 10^8$ s^{-1}; (3) a minor contribution from charge recombination[55,56] to ^{3}Ph-PTZ*, with $k_{CR} = 7.2 \times 10^7$ s^{-1}. Additionally, an ISC process

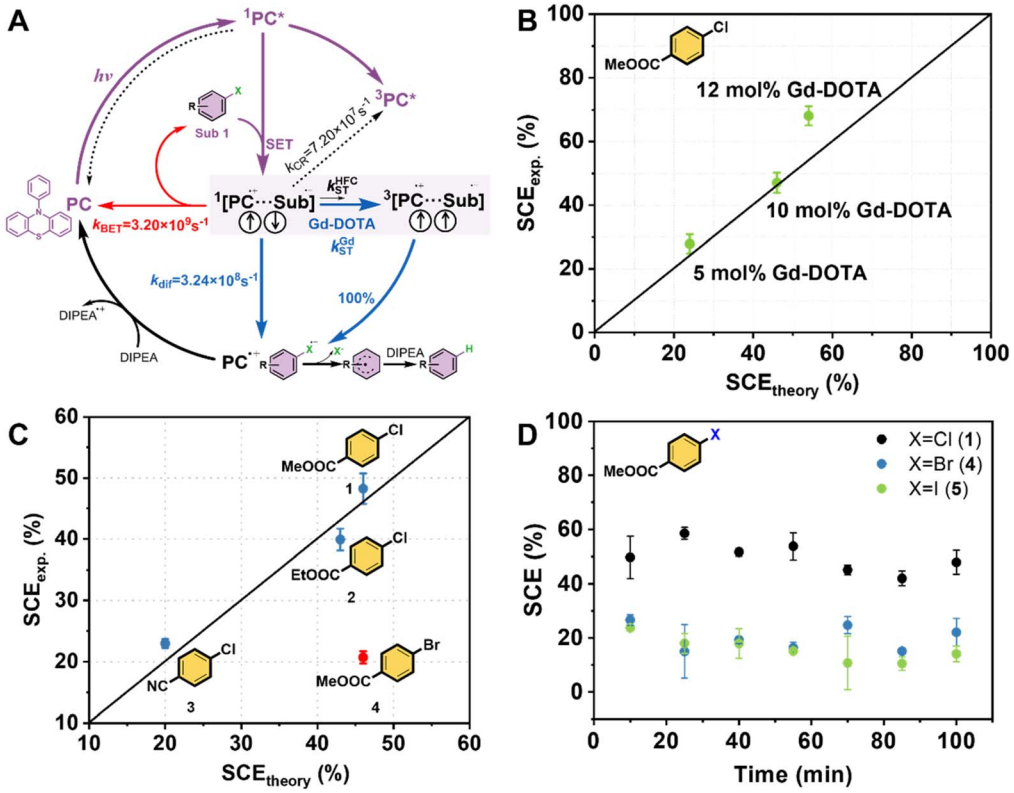

Fig. 5 Kinetic study of SCE. (A) Proposed kinetic mechanism for photoredox cycle between Ph-PTZ and methyl 4-chlorobenzoate. Quantitative validation of SCE *via* comparative analysis between experimental and kinetic model-derived theoretical SCE for varying (B) Gd-DOTA concentrations (5–12 mM) and (C) substrate classes. The black diagonal lines serve as a reference line for an intuitive comparison between the experimental and theoretical values. (D) SCE on substrates with different halogen elements (X = Cl, Br, I) at Gd-DOTA concentration of 10 mM. Reaction conditions: 10 mL reaction solution [DMSO : H_2O = 9 : 1 (v : v)] with 0.1 M methyl 4-chlorobenzoate, 5 mol% PC1 and 2 equiv DIPEA under irradiation by 365 nm LED (4 W cm^{-2}) in air.

from singlet to triplet (S–T) of the RIPs should also exist, though it is indistinguishable from the fs-TA spectra. This special spin-flipping process could be induced by various spin perturbation,[57–61] including hyperfine interaction between the radical electron spin with nuclear spin, SOC of heavy elements, intermolecular spin exchange and dipole interactions with a third paramagnetic center (the ultrafast time-resolved spectroscopy information of Sub 2–4 with Ph-PTZ is shown in Fig. S9). Therefore, paramagnetic Gd-DOTA is expected to introduce a new spin-flipping channel in addition to the "natural" pathways driven by intramolecular magnetic interactions. This leads to a higher population of triplet RIPs, which are less prone to BET due to the Paulin exclusion principle, thereby promoting the effective increase in the final product yield we further performed fs-TA measurements in the presence of Gd-DOTA (Fig. S10). The results revealed a slight increase in the proportion of the cage escape pathway compared to the Gd-DOTA-free case (see Table S1 for details).

Kinetic modeling of spin catalysis effect

With such insight into the reaction mechanism, we proposed a kinetic model to quantitatively reproduce the experimental SCE of Gd-DOTA. In this kinetic scheme, any pathways leading to the formation of free substrate radical is regarded as effective photoredox cycle, and thus the probability of effective reaction without Gd-DOTA, P, is given by the following expression:

$$P = \frac{k_{ST}^{HFC} + k_{dif}}{k_{ST}^{HFC} + k_{dif} + k_{CR} + k_{BET}} = \frac{k_{ST}^{HFC} + k_{dif}}{k_{ST}^{HFC} + k_{RP}} \quad (1)$$

where k_{RP} represents the sum of k_{dif}, k_{CR}, and k_{BET}, as quantified by TAS. k_{ST}^{HFC} represents the theoretical ISC rate of RIPs induced by hyperfine interaction. The structural optimization and spin-density distribution of the radical ions were realized by DFT at UB3LYP/def2-TZVP level. Here, the contribution of SOC is reasonably ignored due to the lack of heavy elements.

Instead, at the presence of Gd-DOTA, the promotion of S–T conversion of RIPs by spin interaction with Gd spin is presumed to be a diffusion-controlled process with a rate constant of k_{ST}^{Gd}. Thus, the effective reaction probability along the spin-catalysis pathway, P^*, is given by:

$$P^* = \frac{k_{ST}^{Gd}[S] + k_{ST}^{HFC} + k_{dif}}{k_{ST}^{Gd}[S] + k_{ST}^{HFC} + k_{RP}} \quad (2)$$

k_{ST}^{Gd} denotes the second-order diffusion rate constant for Gd-DOTA encountering the RIPs and $[S]$ represents the concentration of spin catalyst Gd-DOTA.

Therefore, the theoretical SCE denoting the net promotion of reaction probability by Gd-DOTA in relative to non-catalytic case corresponds to:

$$SCE_{theory} = \frac{P^* - P}{P} \times 100\% \quad (3)$$

Taking Ph-PTZ/Sub 1 system as an example, the intrinsic S–T conversion rate constant of the RIPs, k_{ST}^{HFC}, was calculated to be 1.27×10^8 s^{-1} (Table S2), according to hyperfine coupling mechanism (HFCM) (ref to ST 2). Furthermore, the second-order diffusion-controlled rate constant of Gd-DOTA-mediated spin conversion of RIPs, k_{ST}^{Gd}, was estimated as 2.5×10^{10} M^{-1} s^{-1} (refer to ST 3). Combining k_{dif}, k_{CR} and k_{BET} that were spectroscopically determined above, the theoretical SCE of 5 mol% Gd-DOTA were predicted to be 24%. To our satisfaction, this is in good agreement with the experimental value of 23%. Similarly, the theoretical SCEs for 10 mol% and 12 mol% Gd-DOTA were predicted to be 46% and 54%, respectively, which also well reproduces the experimental results (Fig. 5B). The slight discrepancy between $SCE_{exp.}$ and SCE_{theory} at 12 mol% Gd-DOTA likely arises from enhanced molecular diffusion caused by the elevated temperature required to dissolve this high Gd-DOTA concentration.

To further validate our quantitative model, we expanded the scope of substrates (Sub 1–4, Fig. 5C). The experiments showed that substrates with different substituent characteristics displayed varying SCEs. This variation is primarily attributed to differences in hyperfine coupling strengths and thus the intrinsic k_{ST}^{HFC} of each substrate radical (Table S2). HFC constants for each substrate were obtained by DFT calculations (Fig. S11). The resulting theoretical SCE values for Sub 1–3 closely match the experimental values with 10 mol% Gd-DOTA. These findings confirm the plausibility and effectiveness of the spin catalytic mechanism involving Gd-DOTA and our kinetic model.

Interestingly, upon substituting the Cl atom in Sub 1 with Br and I (yielding Sub 4–5), a much lower SCE was observed experimentally, at only 20% and 15%, respectively (Fig. 5D). This reduction is primarily attributed to the heavy atom effect (HAE)[62–67] of Br and I, which induces strong SOC and thus enhances the intrinsic ISC rate of RIPs, in addition to the HFC contribution. This effect diminishes the relative contribution of the Gd spin to the overall spin decay rate of RIPs, ultimately lowering the apparent SCE. Notably, the observation that the theoretical prediction based solely on HFCM overestimated the SCE values for these substitutions (Fig. 5C) further supports this hypothesis. Similar experimental results showing reduced SCE due to heavy atom introduction were also observed for Sub 6–8 (Fig. S12). Gd-DOTA may also influence the photocatalytic performance by modulating the electronic properties of the substrates, such as reduction potentials, *via* intermolecular interactions. Nevertheless, comparative cyclic voltammetry measurements of the substrates, conducted both in the presence and absence of Gd-DOTA, showed virtually unchanged reduction potentials, effectively ruling out this possibility (Fig. S13).

Synthetic applications

To further assess the broader applicability of spin catalysis in photoredox organic transformations, we investigated prolonged reaction durations (5–10 hours) using optimized catalyst loadings (10 mol% for both Ph-PTZ and Gd-DOTA). As summarized in Table 2, the Gd-DOTA-mediated system exhibited superior catalytic efficiency across all substrates within limited reaction time compared to non-spin-catalytic analogues. Notably, six substrates achieved over 90% conversion, reaching a maximum of 96.3% for

Table 2 Substrate scope of spin catalysis

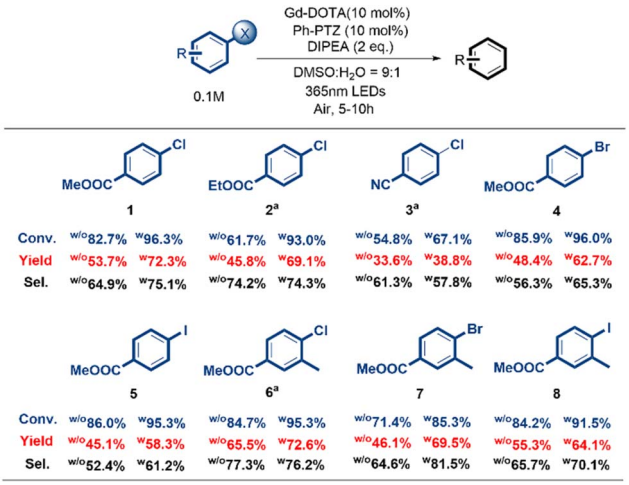

[a] The substrates react for 10 h each, while the remaining substrates react for 5 h each. Note: the blue, red and black font represent the conversion, yield and selectivity without (w/o) or with (w) Gd-DOTA, respectively.

Sub 1. Meanwhile, the hydrodehalogenated product yields also demonstrated substantial enhancements. Furthermore, the product selectivity, defined as yield-to-conversion ratio, remained barely changed or slightly enhanced with the addition of Gd-DOTA, substantiating the mechanistic robustness of spin catalysis. Such invariation in selectivity supports the pure spin-modulation role of Gd-DOTA in promoting the cage escape efficacy of RIPs without chemical affecting the subsequent reaction pathways involving escaping free radicals.

Conclusions

In summary, this study demonstrates a spin modulation strategy for promoting photoredox catalysis using a paramagnetic complex. Experimental results show that the stable Gd-based spin catalyst, Gd-DOTA, effectively facilitates the spin conversion of singlet RIP intermediates, generated *via* SET quenching of the singlet-excited organic photosensitizer by substrates, into the triplet state. This mechanism suppresses BET and thus significantly enhances the forward reaction, yielding a pronounced positive SCE. A kinetic model derived from time-resolved spectra revealed a strong correlation between the SCE and reaction parameters, such as hyperfine coupling strength and diffusion rate constants. These findings highlight paramagnetic spin catalysts as powerful tools to enhance photoredox organic transformations. Through further modification and regulation of spin catalysts, even greater SCEs may be achieved, which could pave the way for impactful applications in fields such as photocatalysis, organic radical transformations, and biocatalysis.

Author contributions

Z. Q. D. responsible for experimental design and implementation, data collection and analysis, drafting the initial manuscript, and performing revisions; C. L. C. conducted time-resolved spectroscopy experiments and data collection; L. F. C. performed DFT calculations; M. L. S., J. Z. Z., S. Z., L. J. C. and J. Y. L. provided support for the experiments, contributed technical assistance to the theoretical aspects of the study, and participated in results discussions. S. M. B. is responsible for the theoretical calculations, analysis, and manuscript revision. J. L. J. is responsible for the experimental testing, data analysis of the ultrafast spectroscopy part and manuscript revision. L. N. Z. is responsible for the overall design and direction of the research, proposing the main research framework and core methodology, applying for and managing research funding, result analysis, and manuscript revision. Additionally, S. G., H. M. S. and the corresponding author provide academic guidance and technical support to all team members. All authors have given approval to the final version of the manuscript.

Conflicts of interest

The authors declare no conflict of interest.

Data availability

All the experimental data related to this work can be found in the SI. See DOI: **https://doi.org/10.1039/d5sc03124a**.

Acknowledgements

We wish to thank our colleagues, co-workers, and collaborators for the important contributions to the work reported herein, particularly thank Dr Yan Duan for immense help with the instrumentation and characterization. This research is supported by the Ministry of Science and Technology of China (No. 2022YFA1505400), the National Natural Science Foundation of

China (No. 22488101), the Fundamental Research Funds for the Central Universities (No. 2023ZYGXZR002) and GBRCE for Functional Molecular Engineering.

References

1 D. Ravelli, S. Protti and M. Fagnoni, Carbon–Carbon Bond Forming Reactions via Photogenerated Intermediates, *Chem. Rev.*, 2016, **116**, 9850–9913.
2 M. Nakajima, E. Fava, S. Loescher, Z. Jiang and M. Rueping, Photoredox-Catalyzed Reductive Coupling of Aldehydes, Ketones, and Imines with Visible Light, *Angew. Chem., Int. Ed.*, 2015, **54**, 8828–8832.
3 M. A. Ischay, M. S. Ament and T. P. Yoon, Crossed intermolecular [2 + 2] cycloaddition of styrenes by visible light photocatalysis, *Chem. Sci.*, 2012, **3**, 2807–2811.
4 T. P. Yoon, M. A. Ischay and J. Du, Visible light photocatalysis as a greener approach to photochemical synthesis, *Nat. Chem.*, 2010, **2**, 527–532.
5 Y. Xi, H. Yi and A. Lei, Synthetic applications of photoredox catalysis with visible light, *Org. Biomol. Chem.*, 2013, **11**, 2387–2403.
6 M. Reckenthäler and A. G. Griesbeck, Photoredox Catalysis for Organic Syntheses, *Adv. Synth. Catal.*, 2013, **355**, 2727–2744.
7 C. K. Prier, D. A. Rankic and D. W. C. MacMillan, Visible Light Photoredox Catalysis with Transition Metal Complexes: Applications in Organic Synthesis, *Chem. Rev.*, 2013, **113**, 5322–5363.
8 J. Xuan and W.-J. Xiao, Visible-Light Photoredox Catalysis, *Angew. Chem., Int. Ed.*, 2012, **51**, 6828–6838.
9 J. W. Tucker and C. R. J. Stephenson, Shining Light on Photoredox Catalysis: Theory and Synthetic Applications, *J. Org. Chem.*, 2012, **77**, 1617–1622.
10 M. A. Ischay and T. P. Yoon, Accessing the Synthetic Chemistry of Radical Ions, *Eur. J. Org Chem.*, 2012, **2012**, 3359–3372.
11 J. M. R. Narayanam and C. R. J. Stephenson, Visible light photoredox catalysis: applications in organic synthesis, *Chem. Soc. Rev.*, 2011, **40**, 102–113.
12 B. Zilate, C. Fischer and C. Sparr, Design and application of aminoacridinium organophotoredox catalysts, *Chem. Commun.*, 2020, **56**, 1767–1775.
13 Y. Lee and M. S. Kwon, Emerging Organic Photoredox Catalysts for Organic Transformations, *Eur. J. Org Chem.*, 2020, **2020**, 6028–6043.
14 M. Uygur and O. García Mancheño, Visible light-mediated organophotocatalyzed C–H bond functionalization reactions, *Org. Biomol. Chem.*, 2019, **17**, 5475–5489.
15 S. Sharma and A. Sharma, Recent advances in photocatalytic manipulations of Rose Bengal in organic synthesis, *Org. Biomol. Chem.*, 2019, **17**, 4384–4405.
16 I. K. Sideri, E. Voutyritsa and C. G. Kokotos, Photoorganocatalysis, small organic molecules and light in the service of organic synthesis: the awakening of a sleeping giant, *Org. Biomol. Chem.*, 2018, **16**, 4596–4614.
17 D. Ravelli, M. Fagnoni and A. Albini, Photoorganocatalysis. What for?, *Chem. Soc. Rev.*, 2013, **42**, 97–113.
18 C. S. Ponseca Jr, P. Chábera, J. Uhlig, P. Persson and V. Sundström, Ultrafast Electron Dynamics in Solar Energy Conversion, *Chem. Rev.*, 2017, **117**, 10940–11024.
19 A. W. Rutherford, A. Osyczka and F. Rappaport, Back-reactions, short-circuits, leaks and other energy wasteful reactions in biological electron transfer: Redox tuning to survive life in O2, *FEBS Lett.*, 2012, **586**, 603–616.
20 S. He, Y. Chen, J. Fang, Y. Liu and Z. Lin, Optimizing photocatalysis via electron spin control, *Chem. Soc. Rev.*, 2025, **54**, 2154–2187.
21 W. Wu, B. Yin, W. Peng, Y. Zhao, Z. Zhou, H. Sheng, W. Ma and C. Zhang, Magnetically modulated photochemical reaction pathways in anthraquinone molecules and aggregates, *iScience*, 2021, **24**, 102458.
22 M. Li, S. Wu, D. Liu, Z. Ye, L. Wang, M. Kan, Z. Ye, M. Khan and J. Zhang, Engineering Spatially Adjacent Redox Sites with Synergistic Spin Polarization Effect to Boost Photocatalytic CO2 Methanation, *J. Am. Chem. Soc.*, 2024, **146**, 15538–15548.
23 R. Naaman, Y. Paltiel and D. H. Waldeck, Chiral molecules and the electron spin, *Nat. Rev. Chem.*, 2019, **3**, 250–260.
24 K. S. Pitzer and E. Gelles, Magnetic Catalysis of A Decarboxylation Reaction1, *J. Am. Chem. Soc.*, 1953, **75**, 5132–5133.
25 J. L. Magee, W. Shand Jr and H. Eyring, Non-adiabatic Reactions. Rotation about the Double Bond, *J. Am. Chem. Soc.*, 1941, **63**, 677–688.
26 B. Tamamushi and H. Akiyama, The Paramagnetic Isomerisation of Maleic Acid into Fumaric Acid in Aqueous Solution, *Bull. Chem. Soc. Jpn.*, 1937, **12**, 382–389.
27 A. L. Buchachenko and V. L. Berdinsky, Spin catalysis as a nuclear spin selective process, *Chem. Phys. Lett.*, 1998, **298**, 279–284.
28 B. F. Minaev and H. agren, Spin-catalysis phenomena, *Int. J. Quantum Chem.*, 1994, **57**, 519–532.
29 E. N. Step, A. L. Buchachenko and N. J. Turro, Paramagnetic Interactions of Triplet Radical Pairs with Nitroxide Radicals: An "Antiscavenging" Effect, *J. Am. Chem. Soc.*, 1994, **116**, 5462–5466.
30 N. J. Turro, X. Lei, I. R. Gould and M. B. Zimmt, External magnetic field dependent influence of lanthanide ions on the chemistry of radical pairs in micelles, *Chem. Phys. Lett.*, 1985, **120**, 397–400.
31 D. Koyama, H. J. A. Dale and A. J. Orr-Ewing, Ultrafast Observation of a Photoredox Reaction Mechanism: Photoinitiation in Organocatalyzed Atom-Transfer Radical Polymerization, *J. Am. Chem. Soc.*, 2018, **140**, 1285–1293.
32 K. Shimomaki, K. Murata, R. Martin and N. Iwasawa, Visible-Light-Driven Carboxylation of Aryl Halides by the Combined Use of Palladium and Photoredox Catalysts, *J. Am. Chem. Soc.*, 2017, **139**, 9467–9470.
33 I. Ghosh, R. S. Shaikh and B. König, Back Cover: Sensitization-Initiated Electron Transfer for Photoredox Catalysis, *Angew. Chem., Int. Ed.*, 2017, **56**, 8584.

34 K. Chen, N. Berg, R. Gschwind and B. König, Selective Single C(sp3)–F Bond Cleavage in Trifluoromethylarenes: Merging Visible-Light Catalysis with Lewis Acid Activation, *J. Am. Chem. Soc.*, 2017, **139**, 18444–18447.

35 I. Ghosh and B. König, Chromoselective Photocatalysis: Controlled Bond Activation through Light-Color Regulation of Redox Potentials, *Angew. Chem., Int. Ed.*, 2016, **55**, 7676–7679.

36 D. M. Schultz and T. P. Yoon, Solar Synthesis: Prospects in Visible Light Photocatalysis, *Science*, 2014, **343**, 1239176.

37 M. Goez, C. Kerzig and R. Naumann, An "All-Green" Catalytic Cycle of Aqueous Photoionization, *Angew. Chem., Int. Ed.*, 2014, **53**, 9914–9916.

38 I. Ghosh, T. Ghosh, J. I. Bardagi and B. König, Reduction of aryl halides by consecutive visible light-induced electron transfer processes, *Science*, 2014, **346**, 725–728.

39 K. Targos, O. P. Williams and Z. K. Wickens, Unveiling Potent Photooxidation Behavior of Catalytic Photoreductants, *J. Am. Chem. Soc.*, 2021, **143**, 4125–4132.

40 E. H. Discekici, N. J. Treat, S. O. Poelma, K. M. Mattson, Z. M. Hudson, Y. Luo, C. J. Hawker and J. R. de Alaniz, A highly reducing metal-free photoredox catalyst: design and application in radical dehalogenations, *Chem. Commun.*, 2015, **51**, 11705–11708.

41 N. J. Turro and K. S. Arora, Magnetic effects on photoinduced emulsion polymerization. Effects of lanthanide ion addition, *Macromolecules*, 1986, **19**, 42–46.

42 J. Wang, K. M. Welsh, K. C. Waterman, P. Fehlner, C. Doubleday Jr and N. J. Turro, Dynamics of interaction between a 1,9-biradical and lanthanide ions, *J. Phys. Chem.*, 1988, **92**, 3730–3732.

43 F. Wu, G. Ye, R. Yi, T. Sun, C. Xu and J. Chen, Novel polyazamacrocyclic receptor decorated core–shell superparamagnetic microspheres for selective binding and magnetic enrichment of palladium: synthesis, adsorptive behavior and coordination mechanism, *Dalton Trans.*, 2016, **45**, 9553–9564.

44 M. Ceulemans, K. Nuyts, W. M. De Borggraeve and T. N. Parac-Vogt, Gadolinium(III)-DOTA Complex Functionalized with BODIPY as a Potential Bimodal Contrast Agent for MRI and Optical Imaging, *Inorganics*, 2015, **3**, 516–533.

45 S. Stoll and A. Schweiger, EasySpin, a comprehensive software package for spectral simulation and analysis in EPR, *J. Magn. Reson.*, 2006, **178**, 42–55.

46 M. J. Frisch, G. W. Trucks, H. B. Schlegel, G. E. Scuseria, M. A. Robb, J. R. Cheeseman, G. Scalmani, V. Barone, G. A. Petersson, H. Nakatsuji, X. Li, M. Caricato, A. V. Marenich, J. Bloino, B. G. Janesko, R. Gomperts, B. Mennucci, H. P. Hratchian, J. V. Ortiz, A. F. Izmaylov, J. L. Sonnenberg, D. Williams, F. Ding, F. Lipparini; F. Egidi, J. Goings, B. Peng, A. Petrone, T. Henderson, D. Ranasinghe, V. G. Zakrzewski, J. Gao, N. Rega, G. Zheng, W. Liang, M. Hada, M. Ehara, K. Toyota, R. Fukuda, J. Hasegawa, M. Ishida, T. Nakajima, Y. Honda, O. Kitao, H. Nakai, T. Vreven, K. Throssell, J. A. Montgomery Jr, J. E. Peralta, F. Ogliaro, M. J. Bearpark, J. J. Heyd, E. N. Brothers, K. N. Kudin, V. N. Staroverov, T. A. Keith, R. Kobayashi, J. Normand, K. Raghavachari, A. P. Rendell, J. C. Burant, S. S. Iyengar, J. Tomasi, M. Cossi, J. M. Millam, M. Klene, C. Adamo, R. Cammi, J. W. Ochterski, R. L. Martin, K. Morokuma, O. Farkas, J. B. Foresman and D. J. Fox, *Gaussian 16 Rev. A.03*, Wallingford, CT, 2016.

47 P. J. Stephens, F. J. Devlin, C. F. Chabalowski and M. J. Frisch, Ab Initio Calculation of Vibrational Absorption and Circular Dichroism Spectra Using Density Functional Force Fields, *J. Phys. Chem.*, 1994, **98**, 11623–11627.

48 L. Hermosilla, P. Calle, J. M. García de la Vega and C. Sieiro, Density Functional Theory Predictions of Isotropic Hyperfine Coupling Constants, *J. Phys. Chem. A*, 2005, **109**, 1114–1124.

49 J. D. Currin, Theory of Exchange Relaxation of Hyperfine Structure in Electron Spin Resonance, *Phys. Rev.*, 1962, **126**, 1995–2001.

50 K. M. Salikhov, New Paradigm of Spin Exchange and its Manifestations in EPR Spectroscopy, *Appl. Magn. Reson.*, 2020, **51**, 297–325.

51 P. Li, A. M. Deetz, J. Hu, G. J. Meyer and K. Hu, Chloride Oxidation by One- or Two-Photon Excitation of N-Phenylphenothiazine, *J. Am. Chem. Soc.*, 2022, **144**, 17604–17610.

52 A. Nikolaev, Z. Lu, A. Chakraborty, L. Sepunaru and J. R. de Alaniz, Interconvertible Living Radical and Cationic Polymerization using a Dual Photoelectrochemical Catalyst, *J. Am. Chem. Soc.*, 2021, **143**, 12278–12285.

53 J. A. Christensen, B. T. Phelan, S. Chaudhuri, A. Acharya, V. S. Batista and M. R. Wasielewski, Phenothiazine Radical Cation Excited States as Super-oxidants for Energy-Demanding Reactions, *J. Am. Chem. Soc.*, 2018, **140**, 5290–5299.

54 S. A. Alkaitis, G. Beck and M. Graetzel, Laser photoionization of phenothiazine in alcoholic and aqueous micellar solution. Electron transfer from triplet states to metal ion acceptors, *J. Am. Chem. Soc.*, 1975, **97**, 5723–5729.

55 P. A. Liddell, D. Kuciauskas, J. P. Sumida, B. Nash, D. Nguyen, A. L. Moore, T. A. Moore and D. Gust, Photoinduced Charge Separation and Charge Recombination to a Triplet State in a Carotene−Porphyrin−Fullerene Triad, *J. Am. Chem. Soc.*, 1997, **119**, 1400–1405.

56 K. Schulten, H. Staerk, A. Weller, H.-J. Werner and B. Nickel, Magnetic Field Dependence of the Geminate Recombination of Radical Ion Pairs in Polar Solvents, *Z. Phys. Chem.*, 1976, **101**, 371–390.

57 A. L. Buchachenko, MIE versus CIE: Comparative Analysis of Magnetic and Classical Isotope Effects, *Chem. Rev.*, 1995, **95**, 2507–2528.

58 I. V. Khudyakov, Y. A. Serebrennikov and N. J. Turro, Spin-orbit coupling in free-radical reactions: on the way to heavy elements, *Chem. Rev.*, 1993, **93**, 537–570.

59 U. E. Steiner and W. Haas, Spin-orbit coupling induced magnetic field effects in electron-transfer reactions with

excited triplets: the role of triplet exciplexes and radical pairs in geminate recombination, *J. Phys. Chem.*, 1991, **95**, 1880–1890.

60 O. V. Khavryuchenko, V. D. Khavryuchenko and D. Su, Spin catalysts: A quantum trigger for chemical reactions, *Chin. J. Catal.*, 2015, **36**, 1656–1661.

61 M. A. Anderson, Y. Xu and C. B. Grissom, Electron Spin Catalysis by Xenon in an Enzyme, *J. Am. Chem. Soc.*, 2001, **123**, 6720–6721.

62 M. Mońka, I. E. Serdiuk, K. Kozakiewicz, E. Hoffman, J. Szumilas, A. Kubicki, S. Y. Park and P. Bojarski, Understanding the internal heavy-atom effect on thermally activated delayed fluorescence: application of Arrhenius and Marcus theories for spin–orbit coupling analysis, *J. Mater. Chem. C*, 2022, **10**, 7925–7934.

63 M. Mońka, D. Grzywacz, E. Hoffman, V. Ievtukhov, K. Kozakiewicz, R. Rogowski, A. Kubicki, B. Liberek, P. Bojarski and I. E. Serdiuk, Decisive role of heavy-atom orientation for efficient enhancement of spin–orbit coupling in organic thermally activated delayed fluorescence emitters, *J. Mater. Chem. C*, 2022, **10**, 11719–11729.

64 Q. Peng, H. Ma and Z. Shuai, Theory of Long-Lived Room-Temperature Phosphorescence in Organic Aggregates, *Acc. Chem. Res.*, 2021, **54**, 940–949.

65 Z. Guo, H. He, Y. Zhang, J. Rao, T. Yang, T. Li, L. Wang, M. Shi, M. Wang, S. Qiu, X. Song, H. Ke and H. Chen, Heavy-Atom-Modulated Supramolecular Assembly Increases Antitumor Potency against Malignant Breast Tumors via Tunable Cooperativity, *Adv. Mater.*, 2021, **33**, 2004225.

66 H. Shi, L. Zou, K. Huang, H. Wang, C. Sun, S. Wang, H. Ma, Y. He, J. Wang, H. Yu, W. Yao, Z. An, Q. Zhao and W. Huang, A Highly Efficient Red Metal-free Organic Phosphor for Time-Resolved Luminescence Imaging and Photodynamic Therapy, *ACS Appl. Mater. Interfaces*, 2019, **11**, 18103–18110.

67 J. C. Koziar and D. O. Cowan, Photochemical heavy-atom effects, *Acc. Chem. Res.*, 1978, **11**, 334–341.